Plasma Sci. Technol. **26** (2024) 094007 (10pp) https://doi.org/10.1088/2058-6272/ad5df2

Enhanced degradation of tetracycline by gas-liquid discharge plasma coupled with g-C_3N_4/TiO_2

Zhenhai WANG (王振海), **Zikai ZHOU** (周子凯), **Sen WANG** (王森)* **and Zhi FANG** (方志)

College of Electrical Engineering and Control Science, Nanjing Tech University, Nanjing 211816, People's Republic of China

*E-mail of corresponding author: wang_sen@njtech.edu.cn

Received 2 April 2024, revised 1 July 2024
Accepted for publication 2 July 2024
Published 29 July 2024

Abstract

Plasma-catalysis is considered as one of the most promising technologies for antibiotic degradation in water. In the plasma-catalytic system, one of the factors affecting the degradation effect is the performance of the photocatalyst, which is usually restricted by the rapid recombination of electrons and holes as well as narrow light absorption range. In this research, a photocatalyst g-C_3N_4/TiO_2 was prepared and coupled with gas-liquid discharge (GLD) to degrade tetracycline (TC). The performance was examined, and the degradation pathways and mechanisms were studied. Results show that a 90% degradation rate is achieved in the GLD with g-C_3N_4/TiO_2 over a 10 min treatment. Increasing the pulse voltage is conducive to increasing the degradation rate, whereas the addition of excessive g-C_3N_4/TiO_2 tends to precipitate agglomerates, resulting in a poor degradation efficiency. The redox properties of the g-C_3N_4/TiO_2 surface promote the generation of oxidizing active species (H_2O_2, O_3) in solution. Radical quenching experiments showed that ·OH, hole (h^+), play important roles in the TC degradation by the discharge with g-C_3N_4/TiO_2. Two potential degradation pathways were proposed based on the intermediates. The toxicity of tetracycline was reduced by treatment in the system. Furthermore, the g-C_3N_4/TiO_2 composites exhibited excellent recoverability and stability.

Keywords: gas-liquid discharge, plasma-catalysis, g-C_3N_4/TiO_2, TC degradation

(Some figures may appear in colour only in the online journal)

1. Introduction

Antibiotics are widely used in health care and have become the most important drugs for treating bacterial infections [1]. However, the overuse of antibiotics results in their long-term accumulation in ecosystems, which in turn induces the production of resistance genes that cause damage to human health and the balance of Earth's environment [2]. Traditional physical, chemical and biological approaches for the removal of antibiotics from wastewater still face issues with low reaction rates, secondary pollution and high cost of equipment operation and maintenance [3]. Therefore, the search for eco-friendly and sustainable techniques to remove antibiotics from wastewater is urgently imminent.

Non-thermal plasma (NTP) is an advanced oxidation process (AOP) for contaminant treatment [4–6]. The plasma-liquid interaction generates a mass of aqueous active species (e.g., ·OH, $\cdot O_2^-$, $ONOO^-$, etc.), which can decompose and mineralize organic compounds [7–9]. Recently, research on water treatment by NTP has been explored. Magureanu *et al* [10] employed a pulsed dielectric barrier discharge (DBD) generated at the gas-liquid interface to degrade hexoketone theophylline pharmaceutical compounds, and a degradation

* Author to whom any correspondence should be addressed.

rate of 92.5% was achieved after 60 min of discharge with a corresponding energy yield of 16 g kWh^{-1}. Hu *et al* [11] achieved almost complete degradation of the contaminant sulfamethoxazole by plasma jet treatment after 20 min. Despite the significant progress made in the plasma degradation of antibiotics, the degradation efficiency still requires further enhancement.

The introduction of photocatalysts into the plasma system can further increase the concentration of strongly oxidizing species, thereby enhancing treatment efficiency. During the discharge process, high-energy electrons collide with N_2, O_2 and H_2O, ionizing and generating a large number of excited-state molecules, ions and free radicals, while higher-energy species generate higher-intensity ultraviolet light when they leap to lower-energy states [12, 13]. When light radiation with an energy greater than the energy gap is irradiated onto the photocatalyst, the electrons in its valence band (VB) will be excited to leap to the conduction band (CB), resulting in surface redox [14, 15]. In addition to the direct decomposition of antibiotic molecules [16], the process reacts with H_2O and adsorbed oxygen to generate reactive radicals [17], thereby enhancing the degradation efficiency. TiO_2 is commonly used in energy-related and environmental applications due to its strong oxidation of organic compounds in wastewater, low toxicity and chemical stability [18, 19]. The performance of photocatalysts is restricted by the band gap width, surface area dimensions, and electron-hole recombination rate. Therefore, improving the performance of photocatalysts is a reasonable method to enhance the efficiency of the plasma-photocatalytic system. Researchers have demonstrated that doping metal and nonmetal ions in the photocatalyst can extend the light absorption region to visible-wavelength regions [20–22]. Sharotri *et al* [21] prepared S-doped TiO_2 for plasma degradation of rhodamine 6G. The results showed that the degradation rate increased from 35% to 91.7% compared to that with pure TiO_2. You *et al* [22] found that TiO_2 doped with Fe ions showed higher photo-activity in the visible wavelength band, and the oxytetracycline degradation rate increased by more than 10% compared with pure TiO_2. Constructing a composite photocatalyst to form a special electron transfer pathway represents a highly effective means of inhibiting the recombination of electron-hole pairs and enhancing the performance of the catalyst.

Herein, a Z-type heterojunction photocatalyst (g-C_3N_4/TiO_2) was proposed to be combined with gas-liquid discharge (GLD) for the degradation of TC. This special structure has the capacity to significantly enhance the specific surface area, expands the visible-light response range, and accelerates the transfer and separation of photogenerated charge carriers from the photocatalyst [23]. However, few studies have focused on the effect of g-C_3N_4/TiO_2 in the GLD on antibiotic degradation. Furthermore, the mechanism of the synergy effect between GLD and photocatalysts remains unclear. In this study, a pulsed GLD was employed to combine the synthesized g-C_3N_4/TiO_2 for the tetracycline degradation. XRD, SEM, and XPS were employed to characterize the g-C_3N_4/TiO_2 composite. The influences of applied voltage, working gas and catalyst dosage on system performance were evaluated. The role of active aqueous species in the degradation process was analyzed by quantifying their concentrations. The degradation pathways were inferred through liquid chromatography-mass spectrometry (LC-MS) and the toxicity estimation software tool (T.E.S.T) was used to analyze the toxicity of intermediates.

2. Experimental section

2.1. Chemical reagents

TC ($C_{22}H_{24}N_2O_8$, purity 96%), titanium dioxide ($Ti(SO_4)_2$, purity 96%), ethanol (C_2H_6O, Analytical Grade), melamine ($C_3H_6N_6$, Analytical Grade), indigo disulfonamide sodium (IDS, Analytical Grade), sodium pyruvate (SP, Analytical Grade), isopropanol (IPA, Analytical Grade), uric acid (UA, Analytical Grade), monopotassium phosphate (MP, Analytical Grade) are commercial products of Sinopharm Chemical Reagent Co., which were not purified before the experiment.

2.2. Synthesis of g-C_3N_4/TiO_2

5 g of melamine was calcined to 550 °C in a muffle furnace at 3 °C min^{-1} and then calcined for 180 min. The calcined sample was ground in a ceramic mortar to obtain g-C_3N_4. Then the products were placed in a beaker containing ethanol and subjected to sonication in a water bath for 1.5 h in order to prevent the agglomeration of the particles. An amount of TiO_2 powder was added to achieve a mass ratio of 1:4 (g-C_3N_4:TiO_2). The suspension-containing beaker underwent sonication for 30 min before being moved in a muffle furnace, heating for 2 h under 300 °C. After 10 h of natural cooling, the composite g-C_3N_4/TiO_2 catalyst was obtained.

2.3. Catalyst characterization

The morphology and the lattice spacing of the g-C_3N_4/TiO_2 were examined through high resolution transmission electron microscopy (HRTEM, FEI Tecnai G2 F30). The chemical state and composition of g-C_3N_4/TiO_2 was examined by X-ray photoelectron spectroscopy (XPS, Kratos Axis-ultra Dld, UK). The XPS valence band spectra of g-C_3N_4/TiO_2 were also measured by XPS. X-ray diffraction (XRD, D8 Advance) was employed to characterize the crystal structure of photocatalyst particles.

2.4. Experimental setup of plasma source and tetracycline degradation

Figure 1(a) shows the diagram of GLD generation and diagnosis system, which consists of a power supply, a discharge reactor, a gas distribution system, and discharge diagnosis devices. A pulsed power supply (Xi'an Smart Maple Electronic Technology) is adopted to excite discharge. The

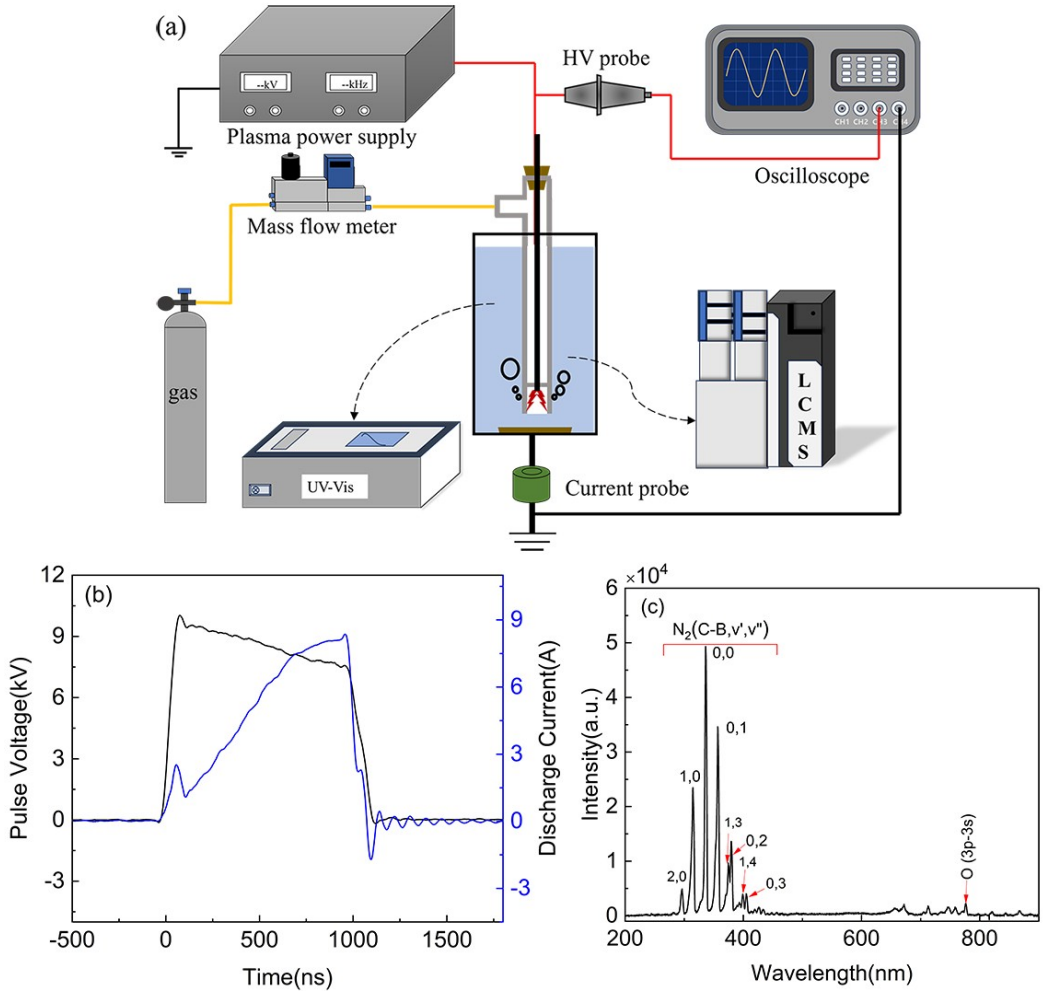

Figure 1. (a) The diagram of GLD generation and diagnosis system, (b) typical *U-I* waveform of gas bubble discharge, (c) typical OES obtained from gas bubble discharge.

power supply is set as a frequency of 1 kHz with a voltage amplitude of 7–10 kV, and both the pulse rising and falling times are 50 ns. A stainless-steel rod (tip radius of curvature: 0.1 mm; diameter: 2 mm) is employed as the high-voltage electrode, which is fixed coaxially in a quartz tube (inner diameter: 8 mm; thickness: 1 mm) with an inlet branch. A cylindrical quartz vessel (height: 100 mm; inner diameter: 60 mm; thickness: 2.5 mm) is employed to hold the tetracycline solution. A stainless-steel plate is placed at the bottom of the quartz tank as a grounding electrode. Figure 1(b) shows the typical *U-I* waveform of the bubble discharge, in which three discharges are observed to occur within one pulse cycle. The average plasma power is estimated to be approximately 42.3 W at a voltage of 10 kV and a frequency of 1 kHz. Optical emission spectrum (OES) of the plasma bubble discharge is shown in figure 1(c). The OES is mainly composed of N_2 ($C^3\Pi_u \rightarrow B^3\Pi_g$, v', v'') and accompanied by the O ($3p^5P \rightarrow 3s^5S$, 777 nm). High-energy electrons are excited by collision with the nitrogen molecule N_2 (X) in the ground state to form the excited states N_2 (A), N_2 (B), and N_2 (C). O ($3p^5P$) is produced through the dissociation of high-energy electrons by collision with water molecules. In addition, the dissociation of high-energy electrons by collision with oxygen molecules in the air is also an important pathway for the production of the high-energy state O ($3p^5P$).

The concentration of long-lived reactive species was quantified using a UV-vis spectrophotometer (Jinghua, UV1800, China), as previously described in references [24, 25]. The degradation products at different treatment times are analyzed by liquid chromatography-mass spectrometry (LC-MS, Agilent, 1290UPLC/Q-TOF6550). The toxicity of TC and intermediates was evaluated by the T.E.S.T.

2.5. Analysis method

The TC degradation rate is calculated by equation (1):

$$\eta = \frac{C_0 - C_t}{C_0} \times 100\%, \tag{1}$$

where η is the degradation rate, C_0 (80 mg L^{-1}) represents the initial TC concentration, and C_t (mg L^{-1}) is the TC concentration for the plasma treatment t (min).

The degradation process of TC follows the first-order kinetic equation (2):

$$\ln(C_0/C_t) = kt, \tag{2}$$

where k (min^{-1}) is the first-order kinetic constant, and t (min) is the treatment time.

The plasma power is calculated by equation (3):

$$P = \frac{1}{T}\int_0^T U(t)I(t)\mathrm{d}t, \tag{3}$$

where P (W) is the plasma power, U (V) indicates the pulse voltage, I (A) is the discharge current and T is the pulse cycle.

The energy yield is calculated by equation (4):

$$\mathrm{EY} = \frac{(C_0 - C_t)V}{Pt} \times 6 \times 10^{-2}, \tag{4}$$

where EY (g kWh^{-1}) is the energy yield, V (L) indicates the volume of TC solution.

The synergetic intensity of the GLD with g-C_3N_4/TiO_2 is calculated from equation (5):

$$\mathrm{SF} = \frac{k_{\mathrm{TiO_2+Plasma}}}{k_{\mathrm{TiO_2}} + k_{\mathrm{Plasma}}}, \tag{5}$$

where $k_{\mathrm{TiO_2+Plasma}}$ is the first-order kinetic constant of TiO_2 added to the plasma system, $k_{\mathrm{TiO_2}}$ is the first-order kinetic constant when only TiO_2 is added, k_{Plasma} is the first-order kinetic constant of the plasma treatment alone.

3. Results and discussion

3.1. Catalysts characterization

The crystalline phase of g-C_3N_4/TiO_2 was detected by XRD with the TiO_2 pattern for comparison, as shown in figure 2(a). At 2θ = 25°, 37.8°, 48.1°, 54.4°, 55.2° and 62.5°, five diffraction peaks were observed for both samples, corresponding to the (101), (004), (200), (105), (211), and (204) crystal planes of TiO_2 [26]. This result indicates that the diffraction peaks of TiO_2 planes in the g-C_3N_4/TiO_2 sample are almost unchanged. Furthermore, the composite material exhibits a pronounced new diffraction peak at 2θ = 27.5°, which can be attributed to the (002) planes of the g-C_3N_4 crystal faces [27]. The XRD results prove that the prepared samples are indeed composed of g-C_3N_4 and TiO_2, and that the crystalline structure of TiO_2 is unaltered by the addition of g-C_3N_4. Figure 2(b) displays the TEM images of g-C_3N_4/TiO_2. The g-C_3N_4/TiO_2 composites exhibit a rough surface and a mesoporous structure, thereby providing a substantial number of active reaction sites [28]. The TEM also suggests that lattice structure of TiO_2 is dispersedly loaded onto the g-C_3N_4. The tight contact interface between two materials facilitates the rapid separation of photogenerated carriers [29], thus improving light absorption and favoring the catalytic reaction.

Figure 3 shows the XPS investigation of the g-C_3N_4/TiO_2 surface. The sample shows four characteristic peaks: O 1s, Ti 2p, N 1s and C 1s in figure 3(a). In the C 1s spectrum (figure 3(b)), three peaks appear at the binding energy of 284.6 eV, 286 eV and 288.8 eV, corresponding to the groups of C–C, C–OH and N=C. The peak at 284.6 eV is derived from the coordination of sp^2-hybridized carbon atoms in the nitrogenated carbon [30]. The peak at 286 eV belongs to C–NH_2 group and the peak at 288.8 eV can be assigned to the sp^2-hybridized carbon in the aromatic ring attached to the NH_2 group [31]. In C 1s spectrum, the binding energy of N–C=N peak (288.8 eV) increases 0.4 eV than g-C_3N_4, which is attributed to the intense interaction between two

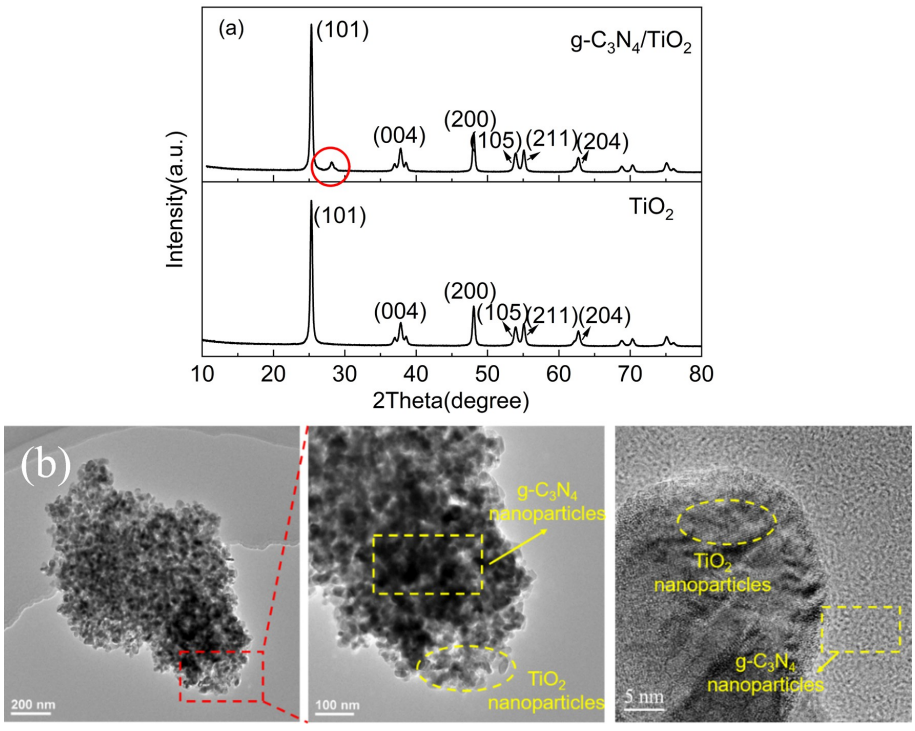

Figure 2. (a) XRD patterns of g-C_3N_4/TiO_2 and TiO_2, (b) TEM images of g-C_3N_4/TiO_2 photocatalyst.

catalysts during high-temperature calcination, leading to the shift in binding energy [32]. Peaks at 529.8 eV and 531.6 eV in figure 3(c) are attributed to O–Ti–O and Ti–O–H, and the oxygen-containing group is favorable for increasing hydrophilicity, thus enhancing the adsorption capacity of g-C_3N_4/TiO_2 on TC molecules in solution [33]. The Ti 2p fine spectrum is split into two peaks at 464.2 eV and 458.6 eV in figure 3(d). It is worth noting that the orbital positions of these two peaks differ by about 5 eV, which suggests that the titanium element in the composite is present as Ti^{4+} [34]. In N 1s spectrum, characteristic peaks at 398.8 eV and 400.1 eV belong to the C–N=C and N–C bonds. The group of C–N=C facilitates the photogenerated electronic transition between g-C_3N_4 and TiO_2 [35].

To determine the band gap and VB position of the prepared sample, UV-vis absorption spectra were performed. Figure 4(a) shows that the absorption wavelength ranges of TiO_2 and g-C_3N_4 are within 450 nm, while g-C_3N_4/TiO_2 shows the broad absorption edge in the 700 nm. The absorption edge of the sample is shifted to higher wavelengths, which indicates that the composite samples significantly improve the utilization of light. The bandgap of three samples was calculated by the Kubelka-Munk function and shown in the inset of figure 4(a) [34, 36]. The bandgap of TiO_2 is 3.23 eV, whereas that of g-C_3N_4/TiO_2 sharply decreases to 2.57 eV. The corresponding VB positions are derived from the VB-XPS spectra, as illustrated in figure 4(b). The VB positions of g-C_3N_4 and TiO_2 are 1.55 eV and 2.77 eV, with calculated CB of −1.02 and −0.46 eV, respectively. A schematic of the g-C_3N_4/TiO_2 structure is illustrated in figure 4(c). It is suggested that photogenerated electrons (e^-) in the $CB_{\text{-TiO2}}$ transfer into $VB_{\text{-g-C3N4}}$ for recombination with h^+, thus inhibiting the electron-hole complexation of TiO_2 [27, 37]. The generated $\cdot O_2^-$, ·OH, and h^+ can act as strong oxidants, accelerating the degradation of TC molecules.

3.2. Degradation of TC by the combination of GLD and g-C_3N_4/TiO_2

The performance of TC degradation by GLD coupled with g-C_3N_4/TiO_2 is evaluated and shown in figure 5. The TC solution treatment volume was 80 mL, the gas flow rate was 0.5 L min^{-1}, the pulse voltage was fixed at 8 kV, and the amount of catalyst added was 0.2 g. It is obviously that GLD/g-C_3N_4/TiO_2 system shows the highest degradation rate. After 10 min of treatment, the GLD/g-C_3N_4/TiO_2 system exhibits a 90.1% degradation of TC, while the GLD/TiO_2 and GLD systems only show 82.9% and 67.3% degradation rates, respectively. As presented in figure 5(b), the reaction rate and energy yield of the GLD/g-C_3N_4/TiO_2 system reach 0.24 min^{-1} and 1.33 g kWh^{-1}, respectively. Therefore, compared to other systems, the GLD/g-C_3N_4/TiO_2 system demonstrates superior degradation performance and energy efficiency. Besides, figures 5(c) and (d) indicate that the highest synergistic factors and TOC removal rate are also observed in the GLD/g-C_3N_4/TiO_2 system, with maximum values of 100% and 35%, respectively.

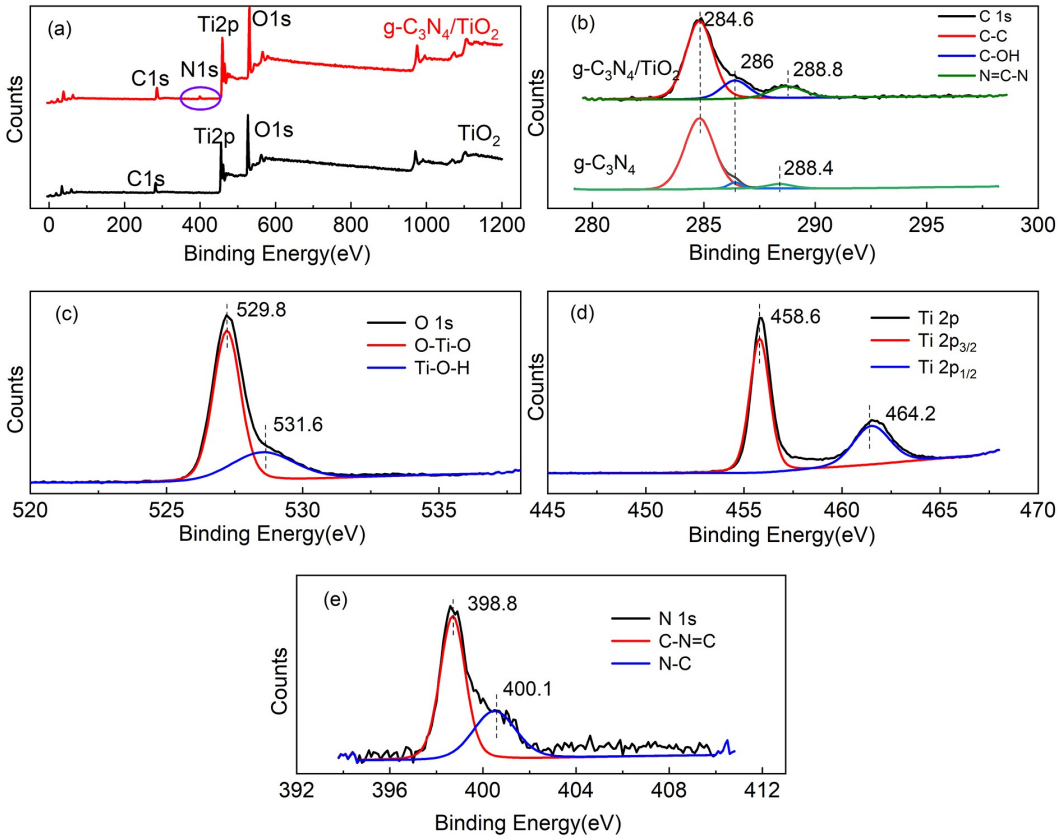

Figure 3. XPS spectrum of g-C_3N_4/TiO_2 composite. (a) Full spectrum, and high-resolution XPS spectra of (b) C 1s, (c) O 1s, (d) Ti 2p, (e) N 1s.

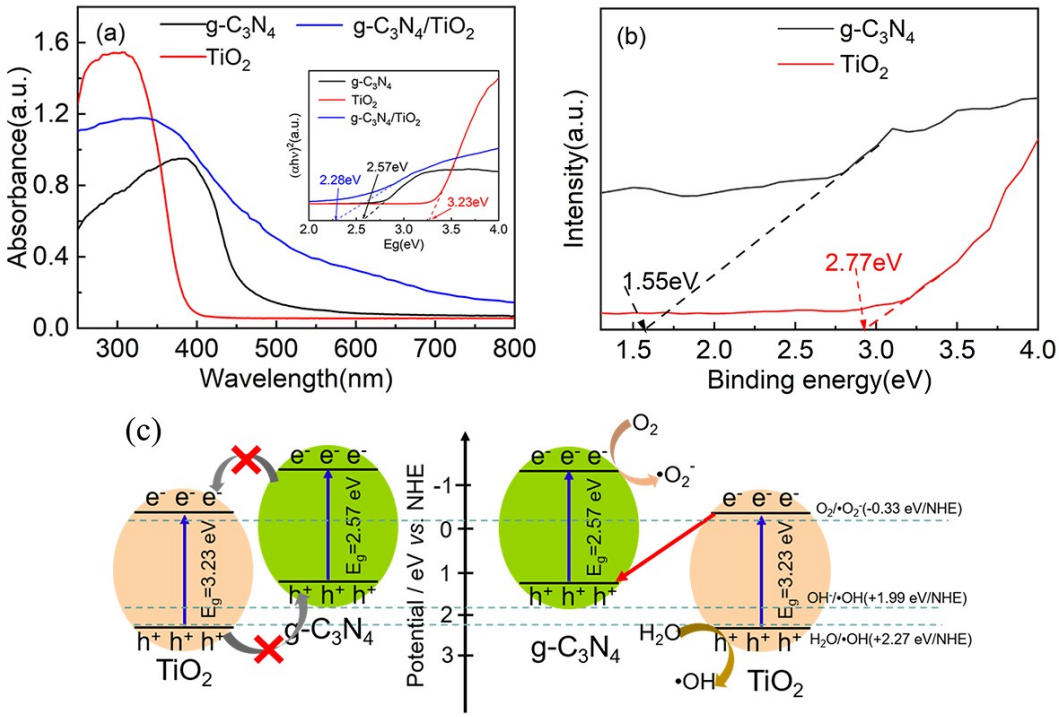

Figure 4. (a) UV-vis diffuse reflectance spectra of g-C_3N_4, TiO_2 and g-C_3N_4/TiO_2 and the corresponding band gap energies (inset), (b) the XPS valence band potential of g-C_3N_4 and TiO_2, (c) transfer pathway of electron and hole in the g-C_3N_4/TiO_2.

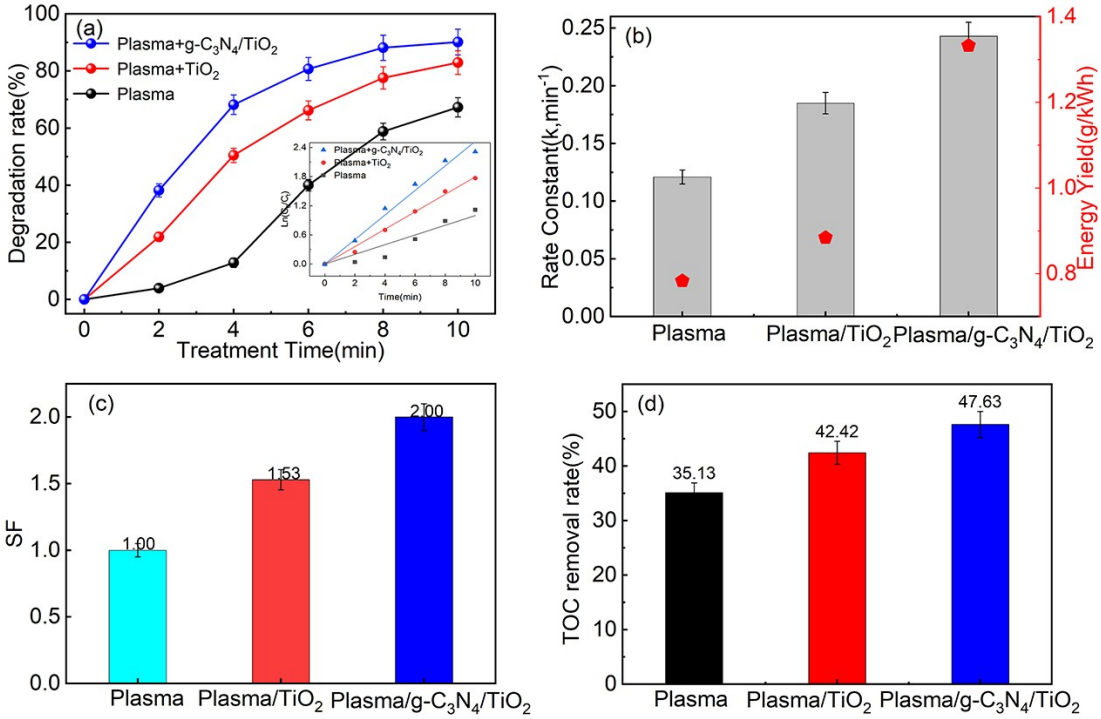

Figure 5. Degradation performance of GLD, GLD/TiO_2, and GLD/g-C_3N_4/TiO_2 systems. (a) Degradation rate, (b) degradation rate and energy yield, (c) synergistic factor, (d) TOC removal rate.

The superior degradation performance of the GLD/g-C_3N_4/TiO_2 system can be attributed to the narrower band gap energy and special electron-hole transfer pathway of g-C_3N_4/TiO_2 [38]. As described in section 3.1, following the excitation of the catalyst by light of a suitable wavelength, $VB_{\text{-TiO2}}$ (2.77 eV) exhibited a more positive potential than H_2O/·OH, and $CB_{\text{-g-C3N4}}$ (−0.33 eV) displayed a more negative potential than O_2/$\cdot O_2^-$ [35], thus the generated h^+ as well as e^- react rapidly with H_2O and O_2 to form ·OH and $\cdot O_2^-$, respectively. Therefore, the GLD/g-C_3N_4/TiO_2 system exhibits superior performance in TC degradation.

The degradation rate obtained from the GLD/g-C_3N_4/TiO_2 system is demonstrated in figure 6(a) as affected by pulse voltage. It is obvious that higher voltages favor TC

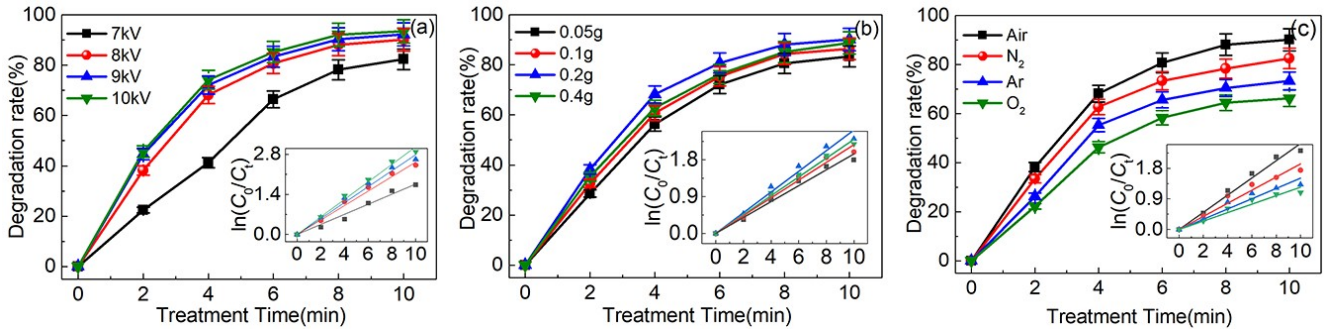

Figure 6. The degradation performance of TC by GLD/g-C_3N_4/TiO_2 under different working conditions. (a) Pulse voltage, (b) catalyst dosage, (c) working gas.

degradation. The degradation rate at 10 min of treatment can be increased by 11.1% when the pulse voltage is applied from 7 kV to 10 kV. Correspondingly, the reaction rate increases from 0.186 min^{-1} to 0.288 min^{-1} (shown in figure 6 (a) inset). An increase in voltage amplitude results in an enhanced discharge, which in turn leads to a further increase in the concentration of reactive oxygen species (ROS) in solution [2, 4, 11]. Additionally, photocatalysts are further activated due to the enhanced light radiation and high-energetic electrons, which results in the generation of more ROS.

Figure 6(b) presents how the degradation rate varies with the catalyst dosage. The degradation rate first increases and then decreases as the dosage of g-C_3N_4/TiO_2 is increased. Following a 10 min treatment, a degradation rate of up to 90.2% was achieved at a dosage of 0.2 g L^{-1}. When the catalyst dosage exceeds 0.2 g L^{-1}, the degradation rate no longer increases but even slightly decreases. As the g-C_3N_4/TiO_2 dosage increases, the contact area between the catalyst and plasma improves. This process can increase the number of active sites [5, 28], thereby facilitating the generation of active species and accelerating antibiotic degradation. An excess of the catalyst dosage will result in a muddy solution, which will scatter and shield light. This phenomenon results in a decrease in the efficiency of the photocatalyst.

Figure 6(c) displays that the degradation rate in the GLD/g-C_3N_4/TiO_2 system varies with the gas type. The air discharge demonstrates the best degradation performance, followed by N_2 conditions and the worst performance under O_2 conditions. After 10 min of discharge treatment, the degradation rate under air discharge conditions reached 90.1% with a maximum reaction rate of 0.243 min^{-1}. In contrast, in O_2 discharge, only 66.2% degradation rate was obtained with a reaction rate of 0.115 min^{-1}. The superior degradation performance under air discharge conditions is attributed to the intense discharge, which efficiently generates reactive oxygen species in plasma and plasma-catalytic reactions. In addition, the presence of reactive nitrogen species during the discharge treatment also facilitates the degradation of antibiotics [39]. Though atmospheric Ar favors the discharge intensity, the hypoxic environment makes ROS generation less efficient. Thus, the production of ·OH radical under conditions of Ar discharge occurs solely as a result of the collision of high-energy electrons or metastable Ar atoms with H_2O molecules [25]. Oxygen, as an electronegative gas, tends to adsorb electrons during pulsed discharges, and therefore the oxygen discharge has the weakest intensity, which is one of the reasons for the lowest degradation efficiency. It should be noted that, according to the optical emission spectra, Ar and O_2 discharges emit light within the 600–900 nm wavelength range [25, 40, 41]. Although g-C_3N_4/TiO_2 is capable of absorbing light within this wavelength range, its efficiency is not comparable to that of UV light [42]. This also provides an explanation for the lower degradation efficiency observed under Ar and O_2 discharge conditions.

3.3. Degradation mechanism

3.3.1. Formation of O_3 and H_2O_2 Figure 7 illustrates O_3 and H_2O_2 concentrations in deionized water (DI) and TC solution. Both H_2O_2 and O_3 concentrations increase gradually with treatment time. The concentration of ROS in GLD-treated TC solutions is found to be lower than that in GLD-treated DI solutions, indicating that O_3 and H_2O_2 are involved in the TC degradation. During TC degradation by long-lived ROS, O_3 directly oxidizes organic macromolecules through the Kerry reaction, electrophilic reaction, and nucleophilic reaction due to its dipolarity, nucleophilic, and electrophilic properties [43]. However, H_2O_2 decomposes into strong oxidizing ·OH through indirect reactions, such as UV decomposition and reaction with O_3 (reactions (6) and (7)), due to its low oxidation potential [4]. In addition, the addition of a g-C_3N_4/TiO_2 catalyst in the GLD system still maintains a high ROS concentration even in the treated TC solution, which is attributed to the new electron migration path, which reduces the recombination rate of electrons and holes. Simultaneous, photo-generated holes in VB-TiO_2 oxidize OH^- or H_2O to produce ·OH (reactions (8) and (9)).

$$H_2O_2 + UV \rightarrow \cdot OH + \cdot OH \quad (6)$$

$$H_2O_2 + 2O_3 \rightarrow 2\cdot OH + 3O_2 \quad (7)$$

$$H_2O + h^+ \rightarrow \cdot OH + H^+ \quad (8)$$

$$OH^- + h^+ \rightarrow \cdot OH \quad (9)$$

3.3.2. The effect of aqueous ROS in TC degradation The contribution of active species in the degradation of TC by the GLD/g-C_3N_4/TiO_2 system was studied, and 50 mM IPA, 10 mM UA, 10 mM MP and 10 mM SP as scavengers of ·OH, O_3, e^*, and H_2O_2 were added, respectively. The reaction rates of IPA with ·OH, MP with e^-, and SP with H_2O_2 were 1×10^9 mol L^{-1} s^{-1}, 1.9×10^7 mol L^{-1} s^{-1} and 1.4×10^6 mol L^{-1} s^{-1} [5, 23, 44]. Figure 8(a) displays the variation of the degradation rate with the addition of different scavengers. Results show that the TC degradation rate is significantly inhibited, specifically 76.4%, 66.5%, 52.4% and 45.4% with the addition of MP, SP, UA and IPA, respectively. The addition of the ·OH scavenger causes the largest decrease of 76.1% in the first-order kinetic constant, from 0.243 min^{-1} to 0.058 min^{-1}. The addition of MP is the least effective in inhibiting TC degradation, with the degradation rate and the first-order kinetic constant decreasing to 45.4% and 0.147 min^{-1}, respectively. The results prove that ·OH is the primary agent responsible for TC degradation. Though hydrated electrons are highly reactive, their role in the plasma-catalytic degradation of TC is insignificant, since they initially react with active species before participating in the degradation of the antibiotic (reactions (10) and (11)) [4, 44].

$$e^* + O_3 \rightarrow O_3^{\cdot -} \quad (10)$$

$$e^* + H_2O_2 \rightarrow \cdot OH + OH^- \quad (11)$$

3.3.3. Degradation pathways of TC The intermediates in the TC degradation by the GLD/g-C_3N_4/TiO_2 system are analyzed by LC/MS. The molecular formulae, molecular mass and molecular structural formulae of the eight intermediates detected are given in table 1. Based on the corresponding intermediates, we propose a reasonable pathway for TC, as demonstrated in figure 9. For pathway I, the C=C band of the TC molecule is first attacked by O_3 or ·OH to form intermediate P1 (m/z = 461). P1 is converted to P3 (m/z = 461) by dehydroxylation. Besides, intermediate P4 (m/z = 395) is produced from the TC molecule by N-demethylation. Intermediate P6 (m/z = 228) is a relatively small intermediate after degradation and is formed by dehydration of P3. In pathway II, the TC molecule readily undergoes dehydration to form P2 (m/z = 428) due to the Keto-Enol Tautomerism on the TC molecule. P2 can be degraded to P5 (m/z = 353) after reactions of N-demethylation [28]. In addition, P7 (m/z = 230) is derived from P4 by dehydration or P5 by N-demethylation. The smaller molecular weight intermediate P8 (m/z = 149) may be derived from P5 by dehydroxylation. With extended treatment times, the TC intermediates will continue to react with ROS, ultimately mineralizing into CO_2 and H_2O.

The toxicity of intermediates during the discharge was tested through the T.E.S.T and the results were represented by mutagenicity and developmental toxicity. Figure 10(a) illustrates that the developmental toxicity of intermediates, with the exception of P2 (0.93), is lower than that of TC (0.86). This indicates that the GLD/g-C_3N_4/TiO_2 system can effec-

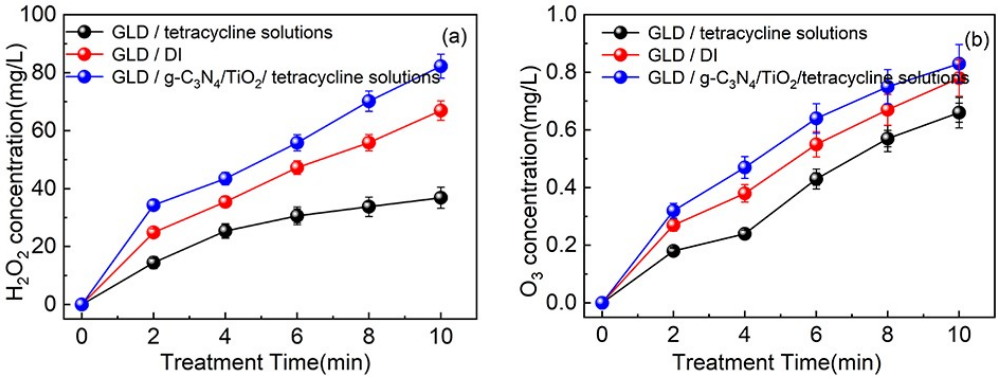

Figure 7. Concentration of reactive oxygen species in the GLD with g-C_3N_4/TiO_2 system. (a) H_2O_2, (b) O_3.

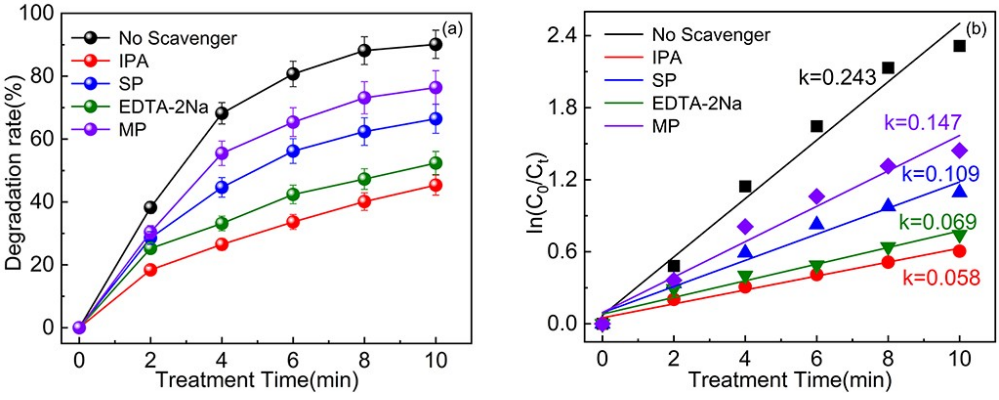

Figure 8. Effect of scavenger on the TC degradation. (a) Degradation rate, (b) reaction rate.

Table 1. The proposed intermediates of TC degradation.

Intermediate	Molecular formula	*m/z*	Structural formula
TC	$C_{22}H_{24}N_2O_8$	445	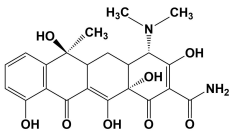
P1	$C_{22}H_{24}N_2O_9$	461	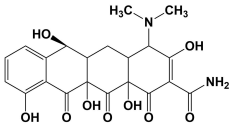
P2	$C_{22}H_{21}NO_8$	427	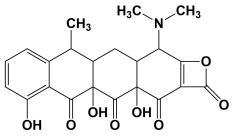
P3	$C_{20}H_{17}NO_{14}$	496	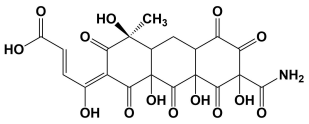
P4	$C_{16}H_{13}NO_{11}$	395	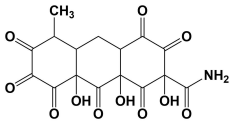
P5	$C_{19}H_{16}O_7$	353	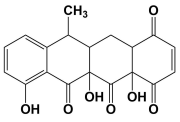
P6	$C_8H_4O_8$	228	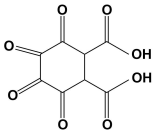
P7	$C_{14}H_{14}O_3$	230	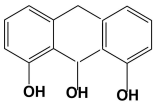
P8	$C_{10}H_{12}O$	149	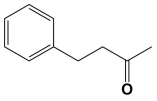

tively reduce the adverse effects of TC on the offspring during the growth and development of individuals [45]. In addition, as shown in figure 10(b), most of the degradation products, including P7 (0.42), P8 (0.09) and P6 (0.02),

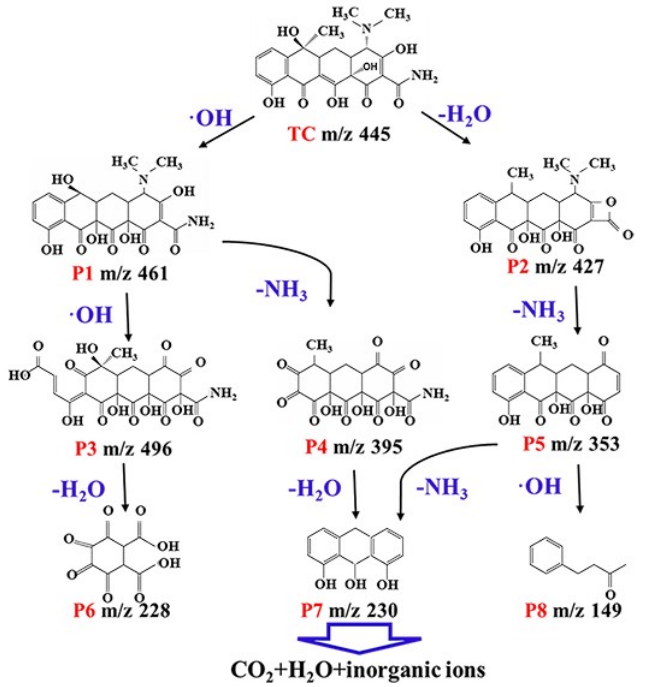

Figure 9. Proposed degradation pathways of TC by GLD synergistic g-C_3N_4/TiO_2 system.

exhibit significantly reduced mutagenicity, which is classified as "mutagenicity negative", in contrast to TC, which is classified as "mutagenicity positive". Following the aforementioned toxicity evaluation, it can be concluded that the residual toxicity of TC treated with the GLD/g-C_3N_4/TiO_2 system is significantly reduced.

3.4. Recoverability and stability of g-C_3N_4/TiO_2

The stability and recoverability of a catalyst are crucial indicators of its performance. As shown in figure 11(a), the degradation rate of TC decreased from 90.1% to 84.3% following five cycles of g-C_3N_4/TiO_2, representing a reduction of approximately 5.8%. Figure 11(b) shows the XRD patterns of both the fresh and used samples of g-C_3N_4/TiO_2. The diffraction peaks of the used sample were in the same position as those of the fresh sample and exhibited similar intensities, indicating that the crystal structure of the g-C_3N_4/TiO_2 composites remained unaltered following repeated use (5 times). In summary, the prepared g-

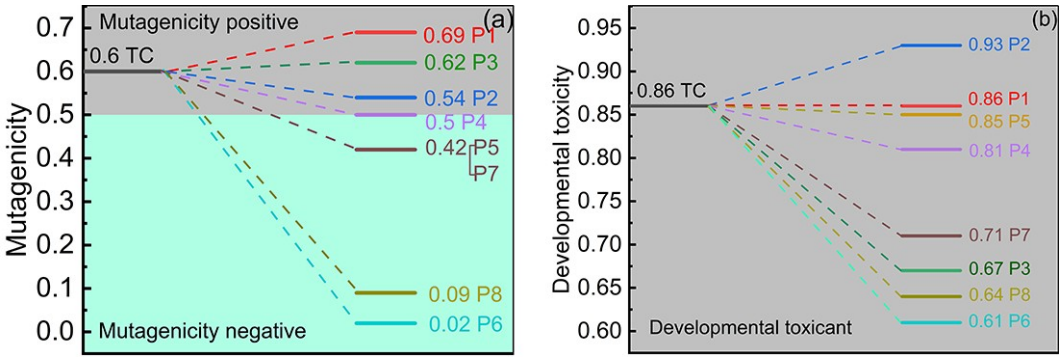

Figure 10. Toxicity of TC degradation intermediates, (a) Mutagenicity, (b) developmental toxicant.

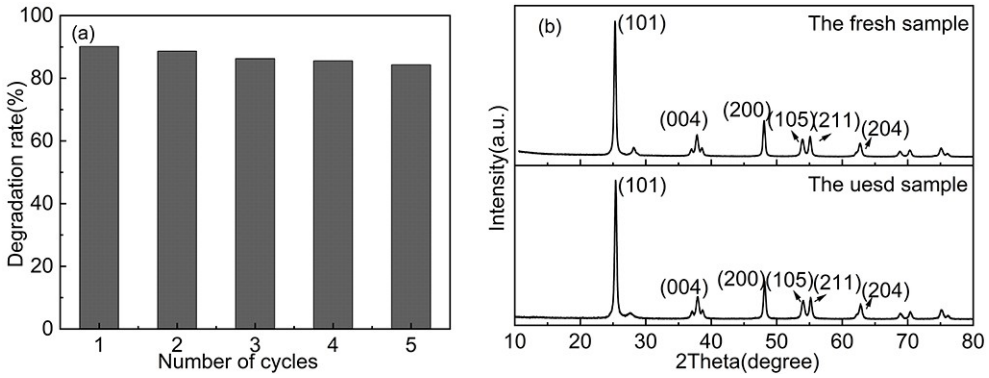

Figure 11. Recoverability and stability of g-C_3N_4/TiO_2. (a) Degradation rate, (b) XRD patterns.

C_3N_4/TiO_2 exhibits excellent stability and recoverability.

4. Conclusion

Briefly, a Z-type heterojunction photocatalyst (g-C_3N_4/TiO_2) was synthesized and introduced into the GLD system to promote the degradation of tetracycline, and the performance of the three systems, GLD, GLD/TiO_2 and GLD/g-C_3N_4/TiO_2, was compared. The degradation rate in the GLD/g-C_3N_4/TiO_2 system reached 90.1% at a 10 min treatment time. The performance of g-C_3N_4/TiO_2 in GLD degradation is significantly affected by pulse voltage, catalyst dosage and working gas. Higher voltage increases the TC degradation rate, while the best degradation performance is achieved when the dosage of g-C_3N_4/TiO_2 is 0.2 g L^{-1} and air is the suitable working gas. Radical quenching experiments proved that ·OH and h^+ are crucial in TC degradation. The degradation pathway is determined by the test of the intermediate products. Toxicity analyses suggest that the toxicity of TC solution is effectively reduced by GLD/g-C_3N_4/TiO_2 treatment. Furthermore, g-C_3N_4/TiO_2 also exhibits excellent stability and recoverability.

Acknowledgment

This work was supported by National Natural Science Foundation of China (Nos. 52277151 and 51907088), Innovative Talents Team Project of 'Six Talent Peaks' of Jiangsu Province (No. TD-JNHB-006).

References

[1] Zhang T Q *et al* 2021 *Chem. Eng. J.* **421** 127730
[2] Hao C J *et al* 2021 *Plasma Sci. Technol.* **23** 115506
[3] Ren J Y *et al* 2019 *Plasma Sci. Technol.* **21** 025501
[4] Wang S *et al* 2022 *Chem. Eng. J.* **450** 138409
[5] Zhou R W *et al* 2021 *Chem. Eng. J.* **403** 126413
[6] Lu F, Zhou J and Wu Z W 2023 *Plasma Sci. Technol.* **25** 035506
[7] Zhang C *et al* 2017 *J. Hazard. Mater.* **326** 221
[8] Johnson M J *et al* 2022 *Plasma Sources Sci. Technol.* **31** 099501
[9] Xu Z Y *et al* 2024 *Plasma Sci. Technol.* **26** 044001
[10] Magureanu M *et al* 2010 *Water Res.* **44** 3445
[11] Hu S H *et al* 2023 *Plasma Sci. Technol.* **25** 035510
[12] Assadi A A, Bouzaza A and Wolbert D 2015 *J. Photochem. Photobiol. A* **310** 148
[13] Assadi A A, Bouzaza A and Wolbert D 2016 *Chem. Eng. Res. Des.* **106** 308
[14] Karoui S *et al* 2022 *J. Water Process Eng.* **50** 103207
[15] Guesmi A *et al* 2022 *Environ. Sci. Pollut.* **29** 55321
[16] Dhibi H *et al* 2023 *J. Water Process Eng.* **53** 103648
[17] Petrović M *et al* 2024 *Plasma Sci. Technol.* **26** 025504
[18] Bogaerts A *et al* 2020 *J. Phys. D: Appl. Phys.* **53** 443001
[19] Yang K *et al* 2022 *Plasma Sci. Technol.* **24** 095504
[20] Liu M M *et al* 2013 *RSC Adv.* **3** 9483
[21] Sharotri N *et al* 2022 *Nanotechnol. Environ. Eng.* **7** 503
[22] You C S *et al* 2022 *Chemosphere* **308** 136163
[23] Li C M *et al* 2018 *ACS Sustain. Chem. Eng.* **6** 16437
[24] Yang D Z *et al* 2021 *J. Phys. D: Appl. Phys.* **54** 244002
[25] Lu X *et al* 2023 *Phys. Chem. Chem. Phys.* **25** 25499
[26] Viet T Q Q *et al* 2021 *Synth. Met.* **280** 116867
[27] Xiao G *et al* 2018 *ACS Nano* **29** 315601
[28] Li G Y *et al* 2022 *Nanomaterials* **12** 2701
[29] Liu Y L *et al* 2021 *RSC Adv.* **11** 4810
[30] Li J H *et al* 2016 *J. Photochem. Photobiol. A* **317** 151
[31] Zhu Y P *et al* 2014 *J. Phys. Chem. C.* **118** 10963
[32] Wei C C *et al* 2021 *Catal. Lett.* **151** 1961
[33] Lu N *et al* 2020 *Chemosphere* **24** 124927
[34] Ki S J *et al* 2019 *Chem. Eng. J.* **377** 120087
[35] Liu X W *et al* 2020 *Chemosphere* **249** 126093
[36] Tan Y J *et al* 2022 *J. Clean. Prod.* **370** 133507
[37] Liu R *et al* 2020 *Energy Technol.* **8** 2000095
[38] Zhou L *et al* 2017 *Res. Chem. Intermed.* **43** 2081
[39] Li W S *et al* 2022 *Chemosphere* **291** 132757
[40] Zhou X F *et al* 2023 *J. Phys. D: Appl. Phys.* **56** 455202
[41] Wang S *et al* 2020 *Plasma Process. Polym.* **18** e2000135
[42] Li H H *et al* 2017 *Appl. Surf. Sci.* **392** 531
[43] Yang T *et al* 2024 *J. Water Process Eng.* **58** 104799
[44] Guo H *et al* 2019 *J. Hazard. Mater.* **371** 666
[45] Xin C H *et al* 2022 *J. Colloid Interf. Sci.* **623** 417